crystals

MDPI

Article

Crystal Structure, Ionic Conductivity, Dielectric Properties and Electrical Conduction Mechanism of the Wyllieites $Na_{1.5}Mn_{3.5}(AsO_4)_3$ and $Na_{1.5}Mn_3Fe_{0.5}(AsO_4)_3$

Eya Rezgui [1], Najoua Ouerfelli [1], S. R. Gavinho [2], J. P. F. Carvalho [2], M. P. F. Graça [2] and S. Soreto Teixeira [2,*]

[1] Laboratory of Materials, Crystallochemistry and Applied Thermodynamics, Faculty of Sciences of Tunis, University of Tunis El Manar, Tunis 1068, Tunisia; eyarezgui24@gmail.com (E.R.); najoua.ouerfelli@fst.rnu.tn (N.O.)

[2] i3N & Department of Physics, University of Aveiro, 3810-193 Aveiro, Portugal; silviagavinho@ua.pt (S.R.G.); jpfc@ua.pt (J.P.F.C.); mpfg@ua.pt (M.P.F.G.)

* Correspondence: silvia.soreto@ua.pt

Abstract: $Na_{1.5}Mn^{II}{}_3Mn^{III}{}_{0.5}(AsO_4)_3$ and $Na_{1.5}Mn^{II}{}_3Fe^{III}{}_{0.5}(AsO_4)_3$ compounds were synthesized via a high-temperature solid-state combustion reaction. The obtained samples were submitted to structural, morphological, and electrical characterizations. X-ray diffraction measurements revealed that both compounds crystallize in the monoclinic system with the space group $P2_1/c$. The lattice parameters were determined to be a = 6.78344 Å, b = 12.93830 Å, c = 11.22825 Å, and β = 98.5374° for $Na_{1.5}Mn^{II}{}_3Mn^{III}{}_{0.5}(AsO_4)_3$, and a = 6.76723 Å, b = 12.9864 Å, c = 11.256 Å, and β = 98.8636° for $Na_{1.5}Mn^{2+}{}_3Fe^{3+}{}_{0.5}(AsO_4)_3$. The structures consist of octahedral Mn^{II} and Mn^{III} or Fe^{III} ions connected by sharing edges, forming infinite chains. These chains are further connected by AsO_4 tetrahedra, resulting in a three-dimensional anionic framework with tunnels parallel to the a-direction and cavities according to the c-direction. The structural models were validated using bond valence and charge distribution analyses. In addition to the structural characterization, the electric results depended on the crystal structures, indicating the potential of the studied materials for being used in several applications.

Keywords: X-ray diffraction; tunnel structure; electrical properties; electric modulus

check for updates

Citation: Rezgui, E.; Ouerfelli, N.; Gavinho, S.R.; Carvalho, J.P.F.; Graça, M.P.F.; Teixeira, S.S. Crystal Structure, Ionic Conductivity, Dielectric Properties and Electrical Conduction Mechanism of the Wyllieites $Na_{1.5}Mn_{3.5}(AsO_4)_3$ and $Na_{1.5}Mn_3Fe_{0.5}(AsO_4)_3$. *Crystals* **2023**, *13*, 1251. https://doi.org/10.3390/cryst13081251

Academic Editors: Andreas Thissen, Fabian I. Ezema and Chinwe Nwanya

Received: 30 June 2023
Revised: 4 August 2023
Accepted: 11 August 2023
Published: 14 August 2023

Copyright: © 2023 by the authors. Licensee MDPI, Basel, Switzerland. This article is an open access article distributed under the terms and conditions of the Creative Commons Attribution (CC BY) license (https://creativecommons.org/licenses/by/4.0/).

1. Introduction

During the last years, thorough research was performed on phosphate and arsenate metal alkaline materials because of their different properties, such as catalytic and optical characteristics [1,2]. Transition metals, especially iron, played an important role in achieving remarkable magnetic features [3]. Monovalent alkaline ions were responsible for ionic conductivity in open framework structures [4–6].

Historically, the mineral wyllieite with the ideal formula $Na_2Fe^{II}{}_2Al(PO_4)_3$ was the first phase described in pegmatites [7]. Later, this type of wyllieite was given the name ferrowyllieiteand. True wyllieite occurs as a Mn^{II} variety, namely, Na_2Mn^{II} $Fe^{II}Al(PO_4)_3$ [8]. Its crystal structure has been interpreted as very close to that of Na_2Mn^{II} (Fe^{II} Fe^{III}) $[PO_4]_3$ [9].

Several minerals of the wyllieite family have been discovered in the last decades. Among them, only three arsenates, $Ag_{1.09}Mn_{3.46}(AsO_4)_3$ [10], $Na_{0.5}K_{0.65}Mn_{3.43}(AsO_4)_3$ [11], and $Na_{1.25}Co_{2.187}Al_{1.125}(AsO_4)_3$, were synthesized. The conduction pathway study of Na^+ in $Na_{1.25}Co_{2.187}Al_{1.125}(AsO_4)_3$ showed that a 1D migration of Na^+ is possible, suggesting a poor ionic conductivity [12]. However, wyllieites may become a valuable source of alkaline conductive materials due to their crystalline structure, which has been interpreted as very close to allaudites [9].

In this context, wyllieite materials were investigated by synthesizing crystallized powders of new $Na_{1.5}Mn^{II}{}_3Mn^{III}{}_{0.5}(AsO_4)_3$ and $Na_{1.5}Mn^{II}{}_3Fe^{III}{}_{0.5}(AsO_4)_3$ compounds.

Initially, Na^+ migration pathways were analyzed using the bond valence sum energy (BVSE) model. The dielectric properties were then examined by complex impedance spectroscopy.

2. Materials and Methods

The crystalline powders of $Na_{1.5}Mn^{II}{}_3Mn^{III}{}_{0.5}(AsO_4)_3$ (I), and $Na_{1.5}Mn^{II}{}_3Fe^{III}{}_{0.5}(AsO_4)_3$ (II) were obtained by a high-temperature solid-state combustion reaction. First, mixtures of $NaNO_3$, $NH_4H_2AsO_4$, $MnCO_3$, and $MnC_6H_9O_6.2H_2O$ for (I) and $Fe(NO_3)_3{\cdot}9H_2O$ for (II) were taken in 1.5:3:3:0.5 stoichiometry. $NH_4H_2AsO_4$, the precursor reagent for As(V), was synthesized by heating As_2O_3 in concentrated nitric acid (HNO_3) under reflux conditions for three days, following a procedure described in previous work [13]. The resulting solution was then taken to further heating at 100 °C until the evaporation of most of the water and excess HNO_3. The resulting $H_5As_3O_{10}$ was calcinated at 300 °C for 12 h to yield As_2O_5. Subsequently, this compound was dissolved in hot water (70 °C) and mixed with an aqueous NH_3 solution to adjust its pH to 4.2. The solid $NH_4H_2AsO_4$ was isolated and confirmed to be phase pure through X-ray diffraction (XRD) analysis using the JCPDS-775 database [14]. The precursors were supplied by Fisher Scientific with a purity percentage of 99%. An amount of 2 g each of the solid mixtures of (I) and (II) were dissolved in 40 mL of water, 10 mL of nitric acid, and 2 g of citric acid. The solutions were placed on a hot plate (maintained at 120 °C), with constant magnetic stirring, to remove excess water. After complete drying, the solid residues were ground manually using an agate vessel and mortar and brought in alumina crucibles at a temperature of 400 °C to promote combustion and remove volatile components. The obtained mixtures of (I) and (II) were then ground for 2 h and brought to 770 °C and 850 °C, respectively, for 24 h.

The data collection of the two materials, $Na_{1.5}Mn^{II}{}_3Mn^{III}{}_{0.5}(AsO_4)_3$ and $Na_{1.5}Mn^{II}{}_3Fe^{III}{}_{0.5}(AsO_4)_3$, was carried out by a diffractometer of the Bruker D8 Advance type. The powdered samples were evenly distributed on a sample holder and rotated during the measurement, applying a 2θ step = 0.017° for material (I) and a 2θ step = 0.015° for material (II). The indexing of all peaks of the materials was carried out by the TREOR program included in X'Pert HighScore software.

The FTIR spectra of pellets composed of KBr mixed with the powder of each sample, in a weight ratio of 200:1 mg, were registered in transmission mode, between 400 and 4000 cm^{-1}, on a Nicolet Avatar 360 spectrometer. Micro-Raman spectroscopy, using a Jobi Yvon spectrometer, was performed at room temperature in backscattering geometry, with the microscope objective (50×) focusing the exciting light (λ = 532 nm) onto the sample (spot diameter < 0.8 μm). Plasma lines were removed by a filter.

The bond valence site energy (BVSE) calculations were performed by the SoftBV program using Na^+ as test ions and 0.1 Å resolution grids [15]. The BVSE isosurfaces were visualized using the VESTA 3 program [16].

To investigate the range of thermal stability of the samples, measurement of thermal gravimetry (TG) and differential thermal analysis (DTA) were performed simultaneously using a Hitachi STA 7300. The measurements were then carried out under a 200 mL/min Nitrogen N50 (99.999%) atmosphere, and the heating rate was set to 10 °C/min [17].

The morphology of the powder grains was observed by scanning electron microscopy (SEM), conducted in a Vega 3 TESCAN SEM microscope. The observed surface of the pellets was previously sputtered with carbon. In order to validate the purity of the two synthesized compounds, the elementary qualitative analysis used an energy dispersion X-ray spectroscopy EDX, using a Bruker system.

In the electrical measurements, the bulk samples had a thickness of 1 mm and a disk shape with a diameter of about 10 mm, prepared by using a steel mold and a uniaxial pressure system applying a pressure of 10 tons for 10 min. The measurements were performed as a function of temperature, in the range of 283 K up to 470 K for the sample $Na_{1.5}Mn^{II}{}_3Mn^{III}{}_{0.5}(AsO_4)_3$ and 296 K up to 393 K for the sample $Na_{1.5}Mn^{II}{}_3Fe^{III}{}_{0.5}(AsO_4)_3$ and frequency (100 Hz up to 1 MHz) using Agilent 4294A impedance analyzer. The

measurements were made in a bath cryostat system, and during the measurements, the samples were in a helium atmosphere [18–20].

3. Results and Discussion

3.1. Resolution and Structure Refinement

Using X'Pert HighScore, it is possible to see that the new phase obtained crystallizes in the monoclinic system $P2_1/c$ isotype to $Ag_{1.09}Mn_{3.46}(AsO_4)_3$ [11]. This structure is then used as a starting model to refine the structure of $Na_{1.5}Mn_2^{III}Mn^{III}_{0.5}(AsO_4)_3$, by substituting Mn for Fe and fixing the occupations to 1. Structure determination was performed using the GSAS program [21]. When refining the structure, the background noise was treated as a polynomial equation and the line profile as a pseudo-Voigt equation. In the end, the goodness of the refinement, $\chi^2 = \left(\frac{R_{wp}}{R_{exp}}\right)^2 = 1.464$, is higher and close to 1, revealing that the refinement quality is good [22]. All atomic positions and thermal site factors were refined. All parameters were refined: R_p (or R-factor) = 0.022, which is a measure of the difference between the observed diffraction pattern and the pattern calculated from the refined crystal structure, R_{wp} (or weighted R-factor) = 0.029, which is similar to R_p but takes into account the weighting of the data points based on their measurement uncertainty, and R_{exp} (or expected R-factor) = 0.025, which measures the agreement between the observed and calculated diffraction patterns, normalized by the number of independent data points and R(F2)= 0.044, which is a measure of the agreement between the observed and calculated structure factors, which are derived from the diffraction pattern. A good superposition between the experimental diffractogram and the refined one was obtained while respecting the chemical reality of the structural model (Figure 1).

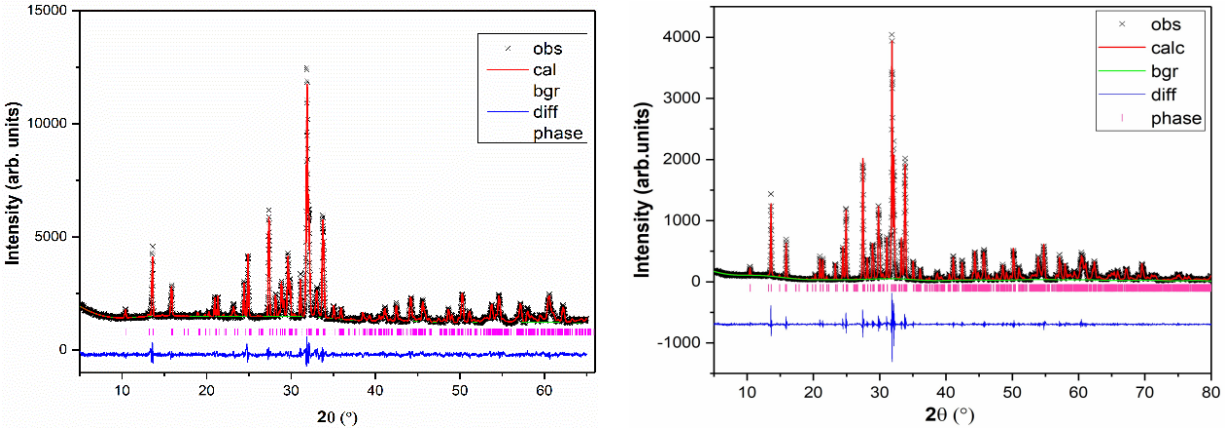


Figure 1. Rietveld plot of the powder X-ray diffraction pattern of (**a**) $Na_{1.5}Mn^{II}_3Mn^{III}_{0.5}(AsO_4)_3$ and (**b**) $Na_{1.5}Mn^{II}_3Fe^{III}_{0.5}(AsO_4)_3$ samples.

Since the goal was to synthesize the isotype phase of $Na_{1.5}Mn^{II}_3Mn^{III}_{0.5}(AsO_4)_3$ by substituting Mn^{III} with Fe^{III}, this structure was used as a starting model to determine and refine the structure $Na_{1.5}Mn^{II}_3Fe^{III}_{0.5}(AsO_4)_3$. Data collection and profile matching were carried out under the same conditions as those for $Na_{1.5}Mn^{II}_3Mn^{III}_{0.5}(AsO_4)_3$. The final results of refinement were χ^2 = 1.440, R_p = 0.083, R_{wp} = 0.105, R_{exp} = 0.088, R(F2) = 0.05682 (Figure 2, Table 1).

3.2. Structures Validation by CHARDI and BVS Analyzes

The two structural models were validated by both analyses: the bond valence (BVS) calculation [23] and the charge distribution method CHARDI [24].

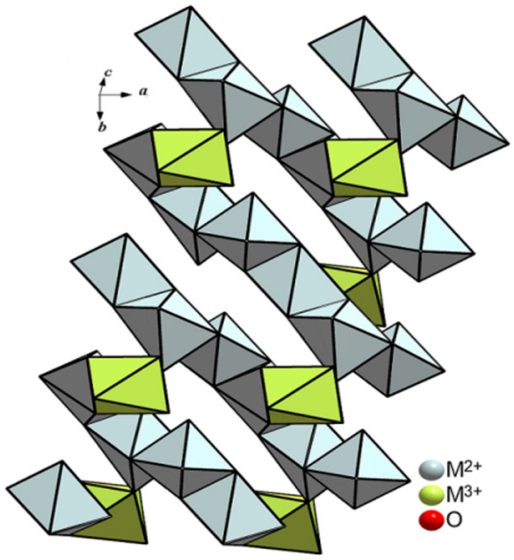


Figure 2. The anionic three-dimensional network formed by octahedral $M^{II}O_6$ and $M^{III}O_6$.

Table 1. Data collection conditions of $Na_{1.5}Mn^{II}{}_3Mn^{III}{}_{0.5}(AsO_4)_3$ and $Na_{1.5}Mn^{II}{}_3Fe^{III}{}_{0.5}(AsO_4)_3$.

Crystal Data		
Formula	$Na_{1.5}Mn^{II}{}_3Mn^{III}{}_{0.5}(AsO_4)_3$	$Na_{1.5}Mn^{II}{}_3Fe^{III}{}_{0.5}(AsO_4)_3$
Molar mass (g/mol)	643.53	643.98
Cristal system, S.G, Z	Monoclinic, $P2_1/c$, 4	
a, *b*, *c* (Å) ; β (°)	6.78344 (9), 12.93830 (15), 11.22825 (19); 98.5374 (19)	6.76723 (12), 12.9864 (3), 11.256; 98.8636 (13)
V (Å^3)	974.54 (2)	977.46 (4)
D_x (g·cm^{-3})	4.386	4.376
Radiation; λ (Å)	Cu K_α (1.54059)	
Data Collection		
Temperature (K)	298(2)	
Diffractometer	D8 Bruker	
Reflection number	4613	1190
2θ (°)	5.028–64.984	5–80
Refinement Results		
R_p	0.022	0.083
R_{wp}	0.029	0.105
R_{exp}	0.025	0.088
$R(F^2)$	0.04407	0.05682
χ^2	1.464	1.440

The CHARDI validation model confirms the two structural models obtained. The charge distribution (Mn^{III}/Mn^{II}) of the Mn cation in material (I) is featured by the dispersion factor on the cationic charges σ_{cat} = 0.079 (Table 2). For material (II), the dispersion factor on the cationic charges is equal to σ_{cat} = 0.045 (Table 3). The values of the CHARDI and BVS calculations (Tables 4 and 5) are in agreement with those observed in the bibliography, presented by the wyllieite $Na_{1.265}Mn^{II}{}_{2.690}Mn^{III}{}_{0.785}(PO_4)_3$ [25].

Table 2. Fractional atomic coordinates, isotropic or equivalent isotropic displacement parameters (Å ^{2}), and Wyckoff positions of material (I).

Atom	x	y	z	Uiso*/Ueq	Wyckoff Positions
As1	0.5824 (3)	0.11275 (14)	0.22827 (18)	0.0277 (6)*	4 *e*
As2	0.8817 (3)	0.39458 (14)	0.26305 (18)	0.0313 (6)*	4 *e*
As3	0.2272 (3)	0.28982 (14)	−0.01591 (18)	0.0114 (6)*	4 *e*
Mn1	0.4139 (3)	0.35341 (14)	0.26964 (18)	0.0216 (6)*	4 *e*
Mn2	0.7199 (3)	0.23080 (14)	0.49625 (18)	0.0092 (6)*	4 *e*
Mn3	0.5	0.0	0.5	0.0491 (6)*	2 *d*
Mn4	0.0827 (3)	0.16419 (14)	0.20656 (18)	0.0217 (6)*	4 *e*
Na1	0.7403 (3)	−0.01431 (14)	0.00492 (18)	0.0139 (6)*	4 *e*
Na2	0.0	0.5	0.0	0.0084 (6)*	2 *c*
O1	0.5503 (3)	0.00107 (14)	0.15914 (18)	0.0787 (6)*	4 *e*
O2	0.7718 (3)	0.17622 (14)	0.17308 (18)	0.0301 (6)*	4 *e*
O3	0.6496 (3)	0.09540 (14)	0.37900 (18)	0.0835 (6)*	4 *e*
O4	0.3917 (3)	0.18877 (14)	0.19837 (18)	0.0217 (6)*	4 *e*
O5	0.0884 (3)	0.33029 (14)	0.26194 (18)	0.0381 (6)*	4 *e*
O6	0.2138 (3)	−0.08500 (14)	0.38092 (18)	0.0405 (6)*	4 *e*
O7	0.0582 (3)	0.00566 (14)	0.15275 (18)	0.0405 (6)*	4 *e*
O8	0.7251 (3)	0.34213 (14)	0.35173 (18)	0.0746 (6)*	4 *e*
O9	0.4129 (3)	0.21657 (14)	−0.04974 (18)	0.0217 (6)*	4 *e*
O10	0.1149 (3)	0.12330 (14)	0.37710 (18)	0.0884 (6)*	4 e
O11	0.3420 (3)	0.38209 (14)	0.07948 (18)	0.0217 (6)*	4 *e*
O12	0.0472 (3)	0.21869 (14)	0.04507 (18)	0.0242 (6)*	4 *e*

Table 3. Fractional atomic coordinates, isotropic or equivalent isotropic displacement parameters (Å ^{2}), and Wyckoff positions of material (II).

Atom	x	y	z	Uiso*/Ueq	Wyckoff Positions
As1	0.5977 (4)	0.1126 (6)	0.2306 (6)	0.0084 (6)	4 *e*
As2	0.890 (1)	0.3943 (5)	0.2631 (5)	0.0228 (5)	4 *e*
As3	0.2385 (2)	0.2885 (5)	−0.0033 (1)	0.0138 (1)	4 *e*
Mn1	0.4150 (3)	0.3469 (3)	0.2808 (1)	0.0043 (1)	4 *e*
Mn2	0.7426 (2)	0.2310 (1)	0.4986 (2)	0.0117 (1)	4 *e*
Fe3	0.5	0	0.5	0.07525	2 *d*
Mn4	0.0797 (8)	0.1575 (5)	0.2096	0.0168 (9)	4 *e*
Na1	0.7676 (2)	−0.0130 (3)	−0.0003 (6)	0.0094	4 *e*
Na2	0	0.5	0	0.04998	2 *c*
O1	0.5563 (4)	0.0035 (5)	0.1576 (7)	0.0502 (4)	4 *e*
O2	0.7559	0.1705 (6)	0.1537 (4)	0.0816 (5)	4 *e*
O3	0.6380 (5)	0.0966 (1)	0.387	0.0184 (6)	4 *e*
O4	0.4055 (6)	0.1882 (8)	0.2151 (4)	0.0092	4 *e*

Table 3. *Cont.*

Atom	x	y	z	Uiso*/Ueq	Wyckoff Positions
O5	0.0942 (6)	0.3214 (8)	0.2731 (1)	0.0336 (5)	4 *e*
O6	0.2627 (7)	−0.0861 (9)	0.3781 (4)	0.0636 (7)	4 *e*
O7	0.0497 (3)	−0.0014 (5)	0.1586 (2)	0.0086 (9)	4 *e*
O8	0.7278 (9)	0.3342 (5)	0.3435 (9)	0.003 (2)	4 *e*
O9	0.4240 (7)	0.2137 (9)	−0.0331 (4)	0.0242 (6)	4 *e*
O10	0.1413 (9)	0.1352 (8)	0.3901 (8)	0.0089 (4)	4 *e*
O11	0.3623 (9)	0.3826 (7)	0.0789 (7)	0.0991 (6)	4 *e*
O12	0.0632 (9)	0.2151 (9)	0.0513 (6)	0.0015 (2)	4 *e*

Table 4. CHARDI and BVS analysis for cations in $Na_{1.5}Mn^{II}_{3}Mn^{III}_{0.5}(AsO_4)_3$. Notes: q(i) = formal oxidation number; Q(i) = computed charge; sof(i) = site occupation factor; CNs = coordination number; ECoN(i) = number of effective coordination.

	BVS Analysis			CHARDI Analysis
Cation	**q(i).sof(i)**	**Q(i)**	**CN(i)**	**ECoN(i)**
Na1	1	1.02	5	5.03
Na2	1	1.01	6	5.53
As1	5.00	4.99	4	3.92
As2	5.00	5.21	4	3.92
As3	5.00	4.83	4	3.95
Mn1	2.00	1.87	6	5.81
Mn2	2.00	2.02	6	5.81
Mn3	3.00	2.74	6	5.29
Mn4	2.00	2.18	6	5.43

Table 5. CHARDI and BVS analysis for cations in $Na_{1.5}Mn^{II}_{3}Fe^{III}_{0.5}(AsO_4)_3$. Notes: q(i) = formal oxidation number; Q(i) = computed charge; sof(i) = site occupation factor; CNs = coordination number; ECoN(i) = number of effective coordination.

	BVS Analysis			CHARDI Analysis
Cation	**q(i).sof(i)**	**Q(i)**	**CN(i)**	**ECoN(i)**
Na1	1	0.91	5	5.18
Na2	1	1.04	6	6.39
As1	5.00	4.98	4	3.87
As2	5.00	5.02	4	3.86
As3	5.00	4.92	4	3.94
Fe	3.00	3.19	6	5.72
Mn1	2.00	1.94	6	5.88
Mn2	2.00	1.88	6	5.85
Mn3	2.00	2.22	6	5.28

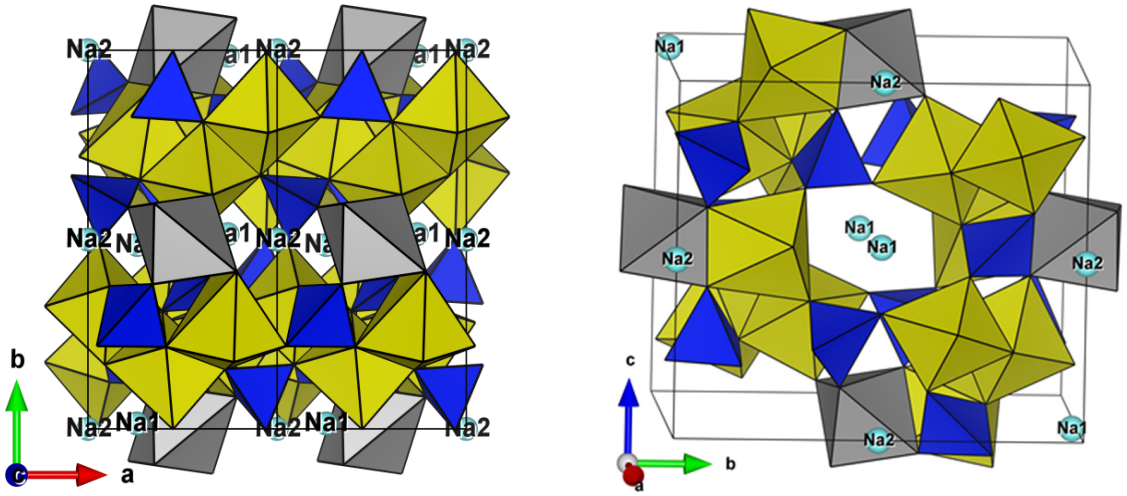
The effective oxidation numbers of Mn(1) (Mn^{II}) and Mn(3) (Mn^{III}) in (I) are 1.87 and 2.74, respectively (Table 2). These values have also been observed in the alliaudyte $Na_{1.72}Mn_{3.28}(AsO_4)_3$, where the effective oxidation numbers of Mn^{II} and Mn^{III} are equal to

1.80 and 2.69, respectively [26]. Indeed, the deviation of the charges on the cations (Mn^{III}, Mn^{II}) in (I) suggests a mixed valence of the trivalent cations Mn^{III} from where the electrons are delocalized in all the three-dimensional networks. However, material (II) did not show any remarkable charge deviations (Table 3).

3.3. Structures Description and Discussion

The asymmetric unit of each compound contains three octahedra of the divalent cation Mn^{II}, one octahedron of the trivalent cation $M^{III}O_6$ (M = Mn or Fe), three tetrahedra AsO_4, and two atoms of Na. The entire group is coordinated by twelve crystallographic independent oxygen atoms.

The three $M^{II}O_6$ octahedra are sharing edges to form the M_3O_{14} group (Figure 2). These groups are connected by sharing edges to form infinite chains in the direction [5,10]. These infinite chains are linked by the tops of the AsO_4 tetrahedra and the edges of the $M^{II}O_6$ octahedra. This arrangement forms a three-dimensional anionic framework containing tunnels parallel to the a-axis and cavities according to the *c*-direction, where sodium cations are located (Figure 3).



(**a**) (**b**)

Figure 3. Projection of the structure (**a**) showing tunnels according to the a-axis, (**b**) showing cavities according to the *c*-direction.

As shown in Table 6, for Mn (1), Mn (2), and Mn (4) in material (I) and Mn (1), Mn (2), and Mn (3) in (II), the MO_6 takes typical M-O distances from those observed in the bibliography. For material (I), Mn^{II}-O distances range from 1.9270 (1) Å to 2.334(2) Å compared with 2.19 Å, which is the sum of the Shannon crystal for Mn^{II} six coordinates (0.97 Å) and O^{2-} three coordinates (1.22 Å), meaning these distances show slight deviations from Mn^{II}-O distances, which range from 1.959 (5) Å to 2.256 (6) Å. This distance variation also shows deviations compared with the sum of the Shannon crystal distances (2.08 Å) [27]. These deviations are observed in most wyllieites, especially $Na_{1.265}Mn^{II}_{2.690}Mn^{III}_{0.785}(PO_4)_3$ [25].

Table 6. M(II)-O and M(III) example distances encountered in weilleytes and alliaudites.

Formula	S.G	M(II)-O (Å)	M(III)-O (Å)	Ref.
$Na_{1.5}Mn_3Fe_{0.5}(AsO_4)_3$	$P2_1/c$	1.959 (5)–2.256 (6)	1.973 (2)–2.040 (3)	*
$Na_{1.265}Mn^{II}_{2.690}Mn^{III}_{0.785}(PO_4)_3$		1.893 (2)–2.334 (2)	2.171 (6)–2.648 (5)	[25]
$Na_{1.5}Mn_3Mn_{0.5}(AsO_4)_3$		1.9270 (1)–2.341 (4)	2.193 (2)–2.4489 (19)	*
$Na_{1.25}Co_{2.187}Al_{1.125}(AsO_4)_3$		1.928–2.151	2.170–2.184	[12]
$Na_2Fe_2^{II}Al(PO_4)_3$		2.089–2.225	1.973	[7]
$Ag_{1.09}Mn_{3.46}(AsO_4)_3$		2.105 (4)–2.413 (5)	1.915 (5)–2.186 (6)	[10]
$Na_{0.5}K_{0.65}Mn_{3.43}(AsO_4)_3$		2.113 (5)–2.46 (5)	1.954 (5)–2.178 (6)	[11]
$NaMn^{II}_{2.5}Fe^{III}_{0.5}Al_{0.5}(PO_4)_3$	$P2_1/n$	2.103–2.245	1.956–2.025	[8]
$K_{1.5}Ni_3\ Fe_{0.5}(PO_4)_3$	$C2/c$	2.0153 (14)–2.2241 (13)	2.016 (2)–2.0490 (13)	[28]
$Na_{1.72}Mn_{3.28}(AsO_4)_3$		2.218 (9)–2.360 (8)	1.990 (12)–2.193 (11)	[26]

* This work

$Mn^{III}O_6$ octahedra in the two studied materials adopt distortions observed previously in $Na_{1.265}Mn^{II}_{2.690}Mn^{III}_{0.785}(PO_4)_3$. The Mn^{III}-O distances in (I) range from 2.193 (2) to 2.4489 (19), while the sum of the Shannon crystalline rays for the Mn^{III} six coordinated ions (0.78 Å) and O^{2-} three coordinated ions (1.22 Å) equals 2.00 Å [27]. The Fe^{3+}-O distances in (II) vary from 1.973(2) Å to 2.040(3) Å, while the Shannon Fe^{3+}-O distance is equal to 2.012 Å [27]. The distortion of the Mn^{III} ion is typical of the distortion phenomenon Jahn–Teller observed in the weillyte $Na_{1.265}Mn^{II}_{2.690}Mn^{III}_{0.785}(PO_4)_3$ [25] and the allyaudite $Na_{1.72}Mn_{3.28}(AsO_4)_3$ [28]. The octahedral $M^{III}O_6$ has four short and two longer $M^{III}O$ distances. The distortion of the $M^{II}O_6$ octahedra and the Jahn–Teller effect of the trivalent cations are consistent with the BVS calculations. This compromise reinforces the mixed valence of $Mn^{II/}Mn^{III}$.

3.4. Infrared Spectroscopy Study

Based on their high intensities and frequencies (Figure 4), the bands around 861 cm^{-1} and 866 cm^{-1} can be attributed to the AsO_4 group asymmetric valence vibrations ν3 in materials (I) and (II), respectively. Symmetrical valence vibrations ν3 are observed around 820–750 cm^{-1} for (I) and around 825–889 cm^{-1} for (II). The asymmetrical deformation vibrations ν4 of the AsO_4 group were observed at the lowest wavelengths. These bands are translated into a wide band divided around 436–371 for material (II) and a band that divides in two around 456–426 cm^{-1} for material (I). The divisions observed in ν1 and ν4 show that the AsO_4 tetrahedrons are minimally deformed in the monoclinic network. The Mn-O vibrations are observed around 538–581 cm^{-1} for (I) and around 583 cm^{-1} for (II). It is also likely that some M^{II}-O strain vibration bands are coupled to the ν4 vibration modes (Table 7).

Table 7. FTIR vibration frequencies (cm^{-1}) attributed to AsO4 tetrahedrons and M-O bonds of some arsenates found in the literature. * This work.

Compound	Valence Vibrations		Deformation		Vibration M-O	Ref.
	ν_1	ν_3	ν_2	ν_4		
(AsO_4)(III)	837	878	349	463	-	[29]
$Na_{0.5}K_{0.65}Mn_{3.43}(AsO_4)_3$	822	880	-	443	564; 420; 669	[11]
$BiCu_6(AsO_4)_3(OH)_6.3H_2O$	848	814; 797	390; 311	553; 529; 494	-	[30]

Table 7. *Cont.*

Compound	Valence Vibrations		Deformation		Vibration M-O	Ref.
	ν_1	ν_3	ν_2	ν_4		
$NaNiFe_2(AsO_4)_3$	860; 901	820; 789; 700	447	496; 474		[31]
$NaCa_2Mg_2(AsO_4)_3$	950; 750		550; 300		-	[32]
$Na_3In_2(AsO_4)_3$	866	934	342	398		[33]
$Na_{1.5}Mn^{II}{}_3Mn^{III}{}_{0.5}(AsO_4)_3$	820; 750	861	-	456; 426	538; 581	*
$Na_{1.5}Mn^{II}{}_3Fe^{III}{}_{0.5}(AsO_4)_3$	825; 889	767	-	436; 371	583	*

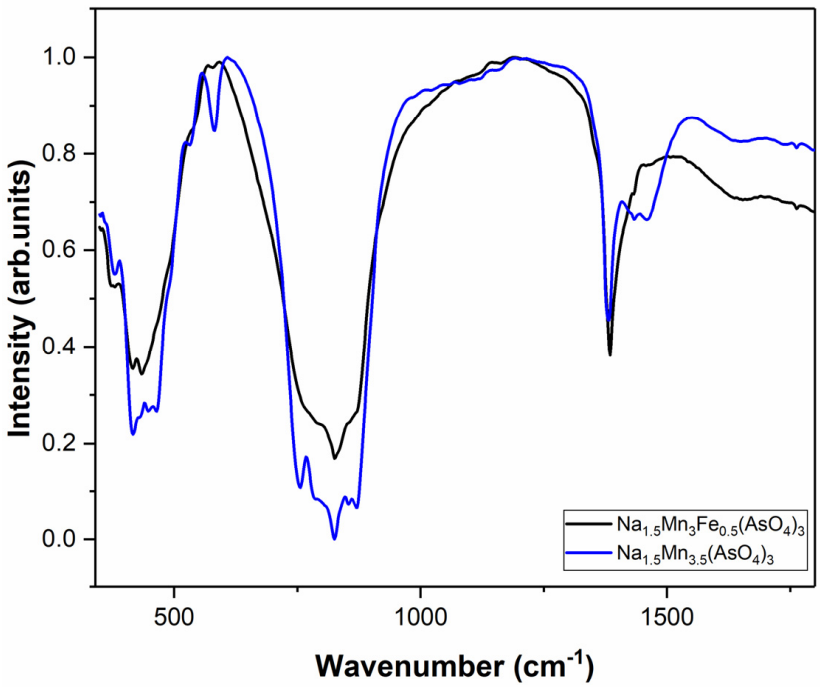


Figure 4. Infrared analysis spectra of compounds (I) and (II).

3.5. Raman Spectroscopy Study

The Raman spectra of the two compounds (I) and (II) in the range 100–1400 cm^{-1} are shown in Figure 5. The Raman spectrum can be understood not only by the determination of the internal vibrations of the $AsO_4{}^{-3}$ units but also by the determination of the vibrations of the crystalline network. In fact, according to the theory of group factors, a material of space group $P2_1/c$ shows 30 bands: 14 corresponding to the symmetry Ag and 16 corresponding to the symmetry Bg. On the other hand, the detection of all bands is difficult because these bands can overlap or have lower intensities than those of background noise [34].

Each spectrum is dominated by a very clear intense band at 838 and 854 cm^{-1} for compounds (I) and (II) respectively. This band corresponds to the symmetrical vibration assignment of the AsO_4^{-3} group (Table 8). The bands observed at 899 and 1000 cm^{-1} correspond to the asymmetric vibration of the $AsO_4{}^{-3}$ group (Table 8). For material (I), five bands of Mn trivalent are observed around 313–358 cm^{-1} and those of divalent are observed around 230–192 cm^{-1}. For material (II), the bands of Fe and Mn are observed around 374 and 256–206 cm^{-1} (Table 8). The superposition of the two Raman spectra showed the same number of bands in the region ranging from 100 to 1250 cm^{-1}. Toward the highest frequencies, it is noticed the appearance of the two broadbands, around 1360 and 1770 cm^{-1}, on the Raman spectrum of (I). These two bands can be attributed to both the D and G vibrations of carbon. Citric acid used for combustion synthesis is the only source

of carbon traces. This phenomenon was observed in the Na_2FePO_4F Raman spectrum, which was prepared by the same synthesis method [34].

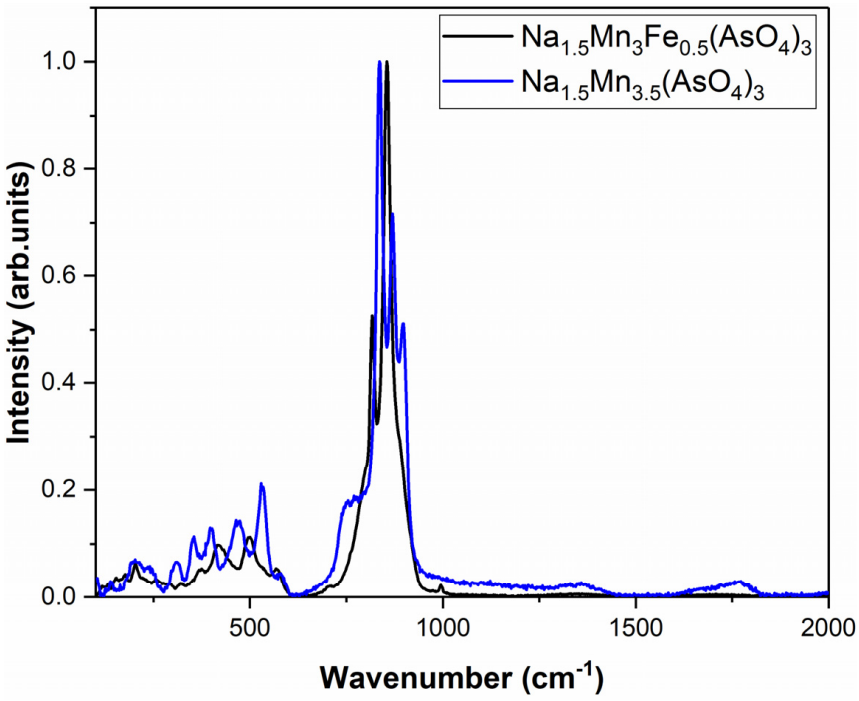


Figure 5. Raman analysis spectra of compounds (I) and (II).

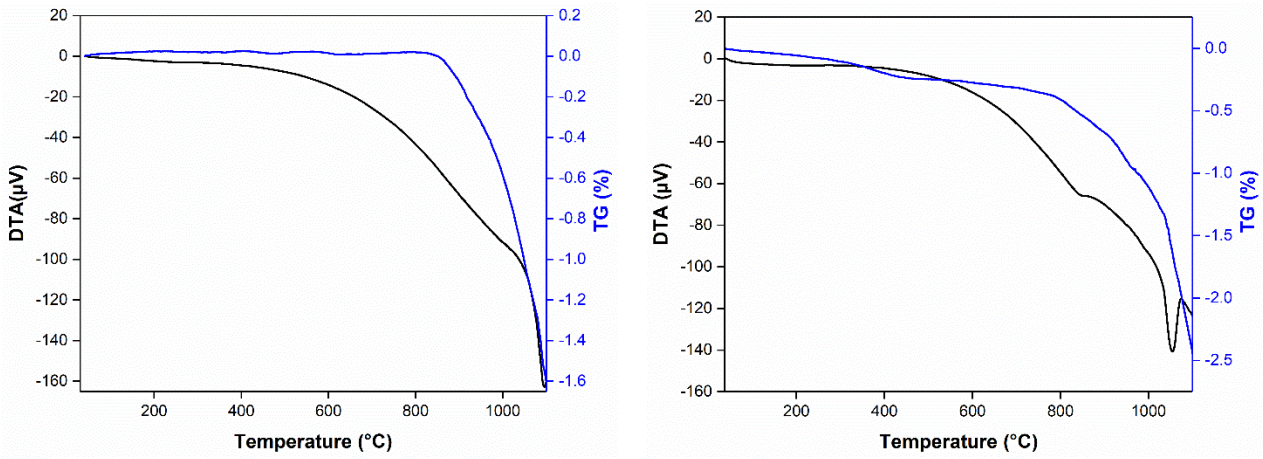
Table 8. Raman vibration frequencies (cm^{-1}) attributed to AsO_4 tetrahedrons and M-O bonds of some arsenates found in the literature (s= symmetric, as = asymmetric).

Compound	ν_1 s	ν_3 as	ν_2 s	ν_4 as	ν_5 M(III)	ν_5 M(II)	Ref.
$Na_{1.5}Fe_{0.5}Mn_3(AsO_4)_3$	854–848–816	1000	417–496	578–569	(Fe) 374	(Mn) 256–206	*
$Na_{1.5}Mn_{3.5}(AsO_4)_3$	838–867–759	899	403–475	529–580	(Mn) 358–313	(Mn) 230–192	*
$Na_7Cu_4(AsO_4)_5$	813–880	902	480–485	511–527	(Cu) 403 334	-	[35]
$Mn_2As_2O_5$	820	900	440	580	-		[36]

* This work.

3.6. Thermal Analysis

The thermal behaviors of both samples, for $Na_{1.5}Mn^{II}{}_3Mn^{III}{}_{0.5}(AsO_4)_3$ and $Na_{1.5}Mn^{II}{}_3Fe^{III}{}_{0.5}(AsO_4)_3$, derived from TG and DTA, are illustrated in Figure 6a,b, respectively. The TGA thermograms show that the compounds are very stable up to 770 °C. The slight loss of mass can be attributed to the thermal volatilization of components. The DTA curves show that both compounds have thermally stable crystal structures. No phase transitions were detected in the range of temperature 50–800 °C. Figure 6b shows a sharp endothermic peak that can be related to the decomposition of the material.

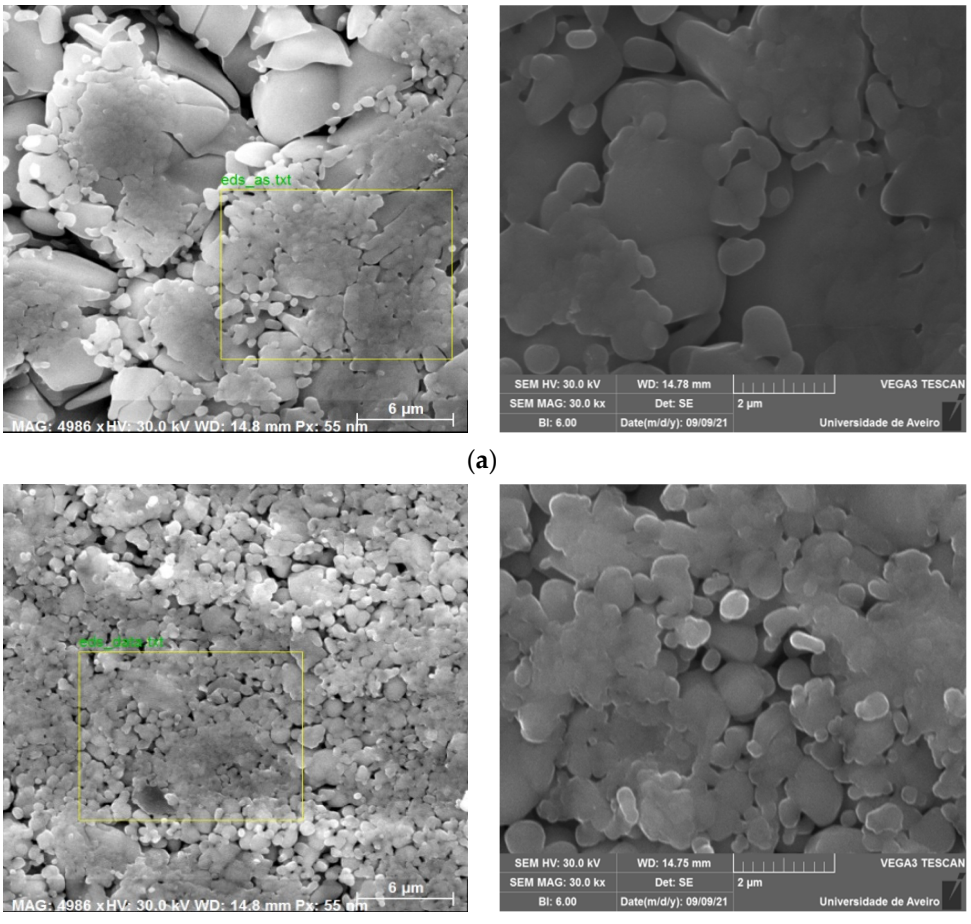


(**a**) (**b**)

Figure 6. TG-DTA curves of (**a**) $Na_{1.5}Mn^{II}_3Mn^{III}_{0.5}(AsO_4)_3$ and (**b**) $Na_{1.5}Mn^{II}_3Fe^{III}_{0.5}(AsO_4)_3$ samples.

3.7. Morphological Analysis

The morphology of the surface of $Na_{1.5}Mn^{II}_3Mn^{III}_{0.5}(AsO_4)_3$ and $Na_{1.5}Mn^{II}_3Fe^{III}_{0.5}(AsO_4)_3$ was examined by SEM. The microstructure observation of both materials showed a homogenous powder. Further observations of the powders showed spherical grains (Figure 7).



(**a**)

(**b**)

Figure 7. SEM micrographs (left figures) and magnifications (right figures) of samples: (**a**) material (I) and (**b**) material (II).

Table 9 shows the elementary composition analysis performed using EDX in both compounds. For compound (I), EDX analysis showed the presence of the elements Na, Mn, As, and O. However, a low-intensity peak was attributed to traces of silicon. The percentages of the detected elements were also in agreement with the crystal structure determined by XRD (Figure 1). For compound (II), Na, Mn, Fe, As, and O elements were detected by EDX analysis. The proportions of the elements detected were consistent with the crystalline structure determined by previous XRD analysis (Figure 1). The source of silicon in material (I) can be attributed to the grinding process using an agate mortar [37].

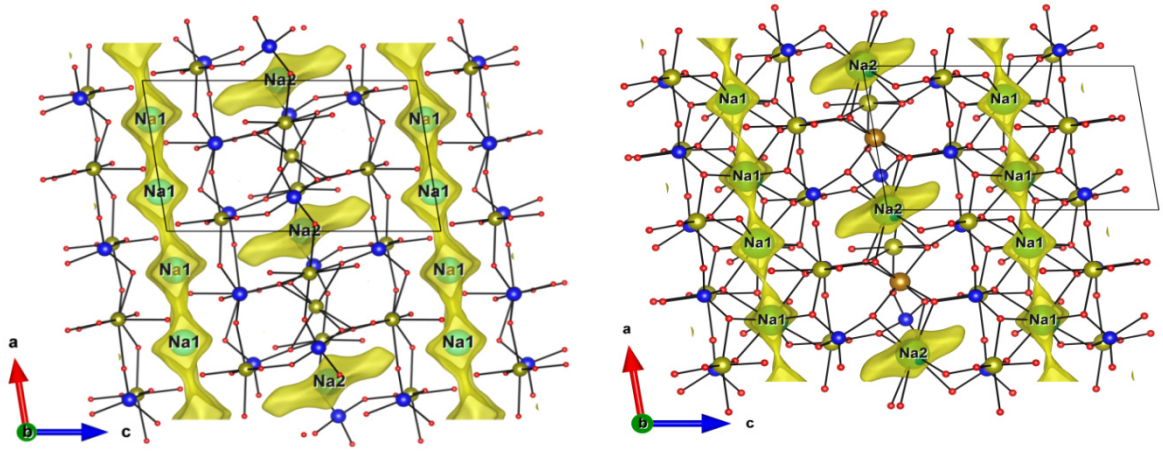
Table 9. EDS semi-quantification results for the elementary atomic percentages.

Material	**$Na_{1.5}Mn^{II}_3Mn^{III}_{0.5}(AsO_4)_3$**		**$Na_{1.5}Mn^{II}_3Fe^{III}_{0.5}(AsO_4)_3$**	
Element	**Experimental**	**Theoretical**	**Experimental**	**Theoretical**
Manganese	20.27%	17.5%	16.75%	15%
Arsenic	16.34%	15%	17.28%	15%
Silicon	1.38%	-	-	-
Sodium	9.33%	7.5%	8.42%	7.5%
Oxygen	52.67%	60%	54.55%	60%
Iron	-	-	3%	2.5%

3.8. Na^+ Pathways Transport Simulation

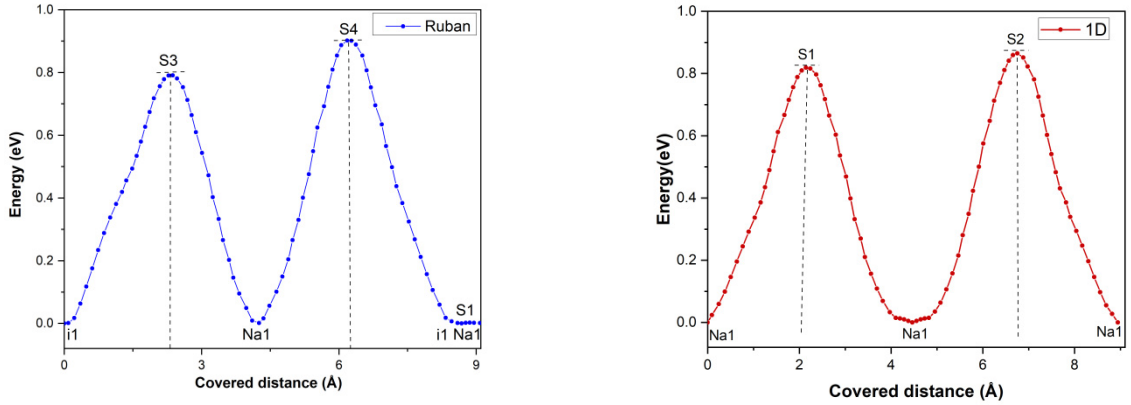
According to the BVSE analysis, this structural study allows for determining the directions of migration. The BVS model is used to verify crystal study suggestions and to determine conduction paths that are not visible during the structural study. Thus, to predict the electrical behavior of both materials, the alkaline migration pathways of Na^+ were simulated using the BVSE model.

Both structures are characterized by tunnels along the a-axis and smaller windows along the *c*-direction. The simulation of the sodium ion conduction paths in the ionic frameworks of (I) and (II) showed that Na(1) can migrate infinitely in the direction (100) in ruban with an E_{mig}= 0.901 eV and 1D with an E_{mig}= 0.865 eV, respectively. However, Na(2) cannot migrate along (001) direction (Figures 8 and 9). The weilliyte $Na_{1.25}Co_{2.187}Al_{1.125}(AsO_4)_3$ BVSE analysis also showed that sodium migration is possible only along the *a*-direction but with higher activation energy of 5.54 eV [12]. In fact, for (I), the diameter of the tunnel sections along the *a*-direction is equal to 4.699 (5) Å, which is slightly less than 4.82 Å, the sum of the diameters of the O^{2-} and Na^+ ions. On the other hand, the section size of the windows according to *c* (3.329 (3) Å) is much smaller than the latter. For (II), the diameter of the tunnel sections is equal to 4.765 (8) Å, which is slightly less than 4.82 Å and the diameter of the tunnel in (II) at the same time. This can explain the higher migration energy of sodium observed in (I). It is noteworthy to point out that the data collection for material (II) involved a greater number of reflections, which enhanced the accuracy of the derived atomic positions of material (I) compared with material (II). For material (I), Na(1) migrated for a 4.257 Å distance from an inertial site i1 to a crystallographic site Na1. At a 2.37 Å distance, Na^+ encountered the saddle S3 with migration energy equal to 0.791 eV. A higher migration energy (E_{mig} = 0.901 eV) was required to enable Na(1) to migrate from its crystallographic site to an interstitial site i1, and only an energy of 0.001 eV was required for the migration of Na(1) from i1 to Na1 sites, which enabled Na(1) to migrate a total distance of 9.701 Å. Figure 8b showed two main bottlenecks for material (II) presented by the two saddles, S1 and S2. In fact, Na(1) traveled first for a 2.146 Å distance from a crystallographic site Na1 to another requiring a migration energy equal to 0.819 eV. Then Na(1) traveled for an 8.691 eV distance encountering the highest migration energy of 0.865 eV arriving at the crystallographic site Na1.



(**a**) (**b**)

Figure 8. (**a**) Migration paths of Na^+ cations in (I) at E_{mig} = 0.901 eV; (**b**) Migration paths of Na^+ cations in (II) at E_{mig} = 0.865 eV.



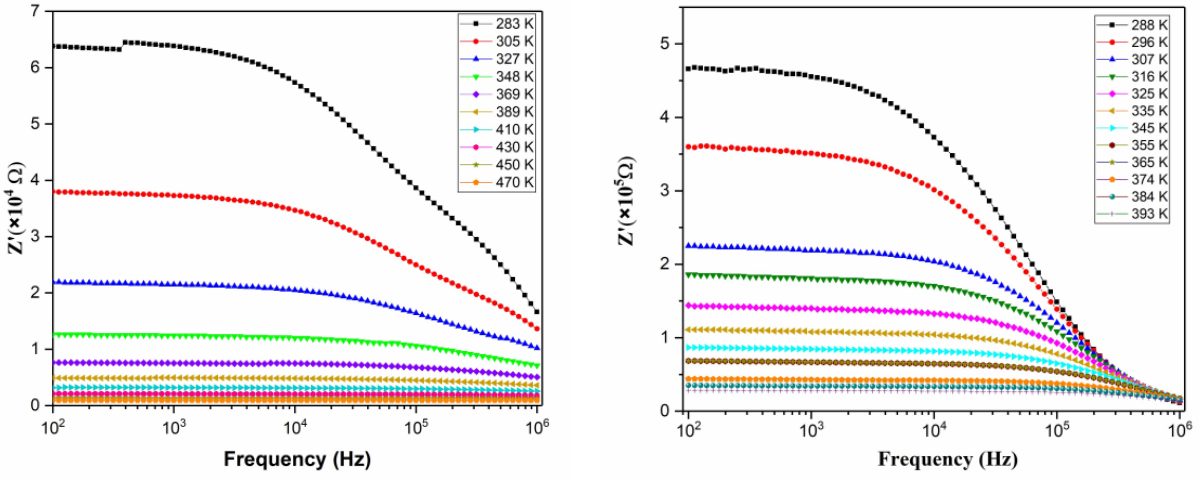
(**a**) (**b**)

Figure 9. Traveled distance variation of Na (1) as a function of migration energy: (**a**) in (I), (**b**) in (II).

3.9. Electrical Measurements

3.9.1. Impedance Analysis

The impedance spectroscopy technique (IS) is frequently employed in experimentation, to explore the electrical characteristics of the ceramic materials. It offers insights into conductivity, relaxation, and permittivity properties. Figure 9 shows the typical complex impedance spectra obtained on heating for $Na_{1.5}Mn^{II}{}_3Mn^{III}{}_{0.5}(AsO_4)$ and $Na_{1.5}Mn^{II}{}_3Fe^{III}{}_{0.5}(AsO_4)_3$. Based on the observed behavior, it can be inferred that there is a correlation between Z′ and the electrical resistance of the sample. As the frequency and temperature increase, the value of Z′ decreases, which is a typical behavior observed in dielectric materials [38]. Additionally, for the $Na_{1.5}Mn^{II}{}_3Fe^{III}{}_{0.5}(AsO_4)_3$ sample, as the frequency increases, the Z′ values at various temperatures converge. This behavior indicates that the energy barrier to be overcome by the charge carriers in this specific experimental condition is very high for the electrical space displacement [37] (Figure 10).



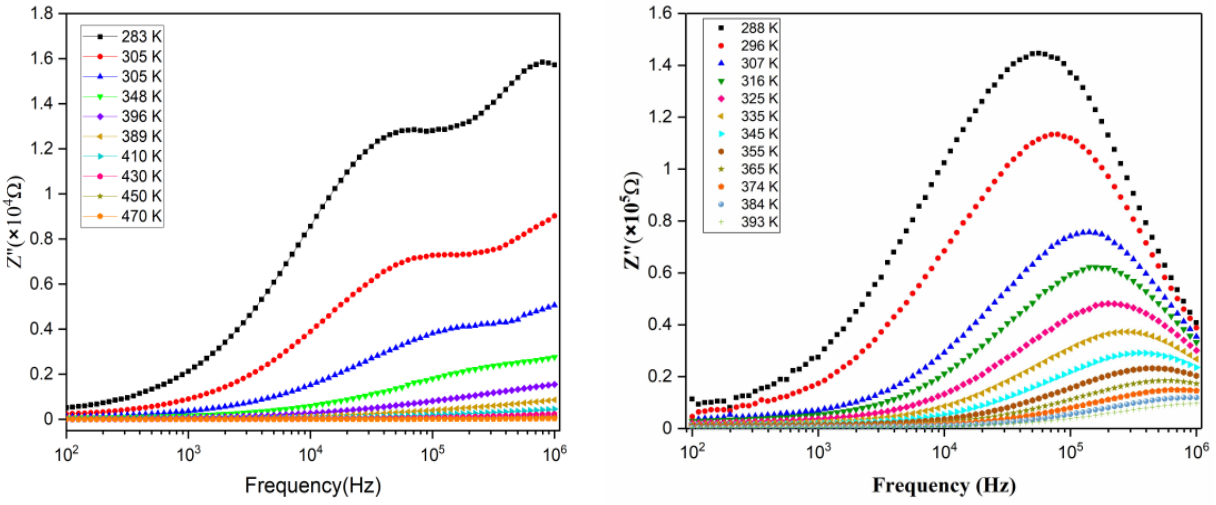
(**a**) (**b**)

Figure 10. The frequency dependence of the real (Z′) part of the complex electrical impedance at several measurement temperatures for (**a**) $sNa_{1.5}Mn^{2+}{}_3Mn^{3+}{}_{0.5}(AsO_4)_3$ and (**b**) $Na_{1.5}Mn^{2+}{}_3Fe^{3+}{}_{0.5}(AsO_4)_3$.

Figure 11 describes the behavior of the imaginary part of impedance Z″ as a function of frequency, for both materials under different temperatures. The plot shows a gradual increase in Z″ with increasing frequency until it reaches a maximum, indicating the presence of a relaxation phenomenon. The peak in Z″ shifts to higher frequencies as the temperature increases, indicating that the resistance of the material is decreasing. At higher frequencies, and for the $Na_{1.5}Mn^{II}{}_3Fe^{III}{}_{0.5}(AsO_4)_3$ sample, Z″ merges for all temperatures, suggesting an accumulation of space charge (Figure 11b). The plot also shows a single relaxation peak that increases with the rise in the temperature, following an Arrhenius behavior [39]. At lower temperatures, the plot of Z″ as a function of frequency for $Na_{1.5}Mn^{II}{}_3Mn^{III}{}_{0.5(}AsO_4)_3$ shows two peaks, which suggests two relaxation processes. The lower-frequency peak can be associated with the bulk resistance of the material, while the higher-frequency peak can be associated with the grain boundary resistance. At low temperatures, the grain boundary resistance dominates, leading to a broad peak in the Z″ spectrum (Figure 11a). For both materials, the maximum value of Z″ decreases with the increase in temperature. These plots further show the spreading of the relaxation time distribution, indicating a temperature-dependent relaxation. The observed broadening of the Z″ peak, with increasing temperature, suggests a thermally activated relaxation process associated with different species, such as electrons or immobile species at lower temperatures and defects at higher temperatures [39].

3.9.2. Modulus Analysis

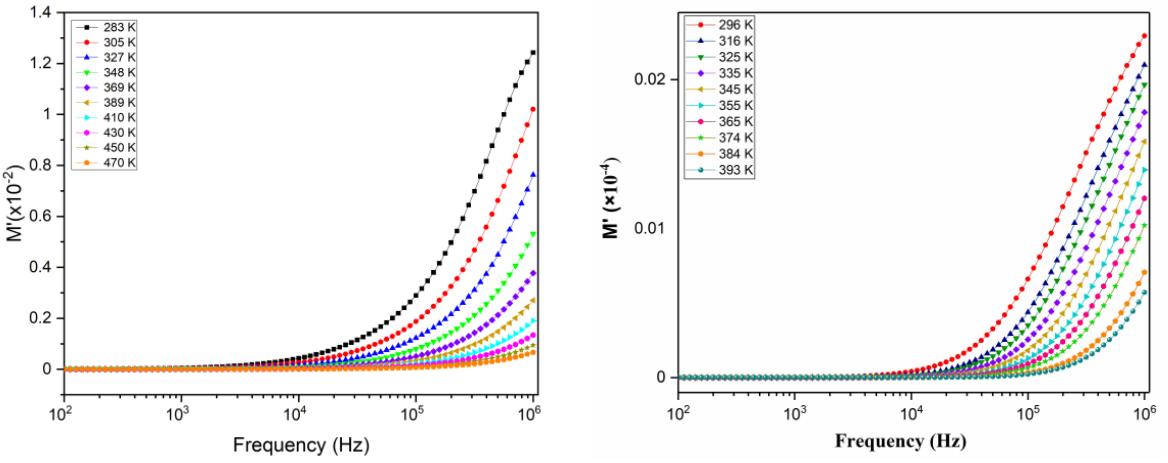
The inverse of the complex dielectric permittivity, ε*, for $Na_{1.5}Mn^{II}{}_3Mn^{III}{}_{0.5}(AsO_4)_3$ and $Na_{1.5}Mn^{II}{}_3Fe^{III}{}_{0.5}(AsO_4)_3$ is known as the complex electric modulus M*. In order to calculate M*, the impedance data was utilized in the following equation: $M^* = 1/\varepsilon^* = M' + jM'' = (Z'' + Z'\omega C)/\omega CZ_0$, where Z′ and Z″ are the real and imaginary parts of the complex impedance Z*, and M′ and M″ are the real and imaginary parts of the complex modulus M*, respectively. Additionally, C_0 represents the vacuum capacitance of the measuring cell, which is determined by the permittivity of the vacuum (ε_0), the cross-section area (S), and the thickness (L) of the sample.



(**a**) (**b**)

Figure 11. The frequency dependence of the imaginary (Z″) part of the complex electrical impedance at several measurement temperatures of (**a**) for $Na_{1.5}Mn^{III}{}_3Mn^{II}{}_{0.5}(AsO_4)_3$ and (**b**) $Na_{1.5}Mn^{II}{}_3Fe^{III}{}_{0.5}(AsO_4)_3$.

Figure 12 shows the variation of the real part of the modulus M′ as a function of frequency for both studied materials at different temperatures. As can be seen at low frequencies, M′ remains consistent and is almost zero at all temperatures. This is due to the lack of restoring force leading to long-range transport of load carriers below the applied ac-electric field. At higher frequencies, M′ increases progressively due to the short-range conduction effects of the Na^+ ions.



(**a**) (**b**)

Figure 12. Frequency dependence of the real part of electric modulus (**a**) for $Na_{1.5}Mn^{2+}{}_3Mn^{3+}{}_{0.5}(AsO_4)_3$ and (**b**) for $Na_{1.5}Mn^{2+}{}_3Fe^{3+}{}_{0.5}(AsO_4)_3$ at different temperatures.

As shown in Figure 13a, the imaginary part of the dielectric modulus of $Na_{1.5}Mn^{II}{}_3Mn^{III}{}_{0.5}(AsO_4)_3$, M″, increases continuously with the frequency, indicating that the material has a high capacity for energy storage and low capacity for dissipation. This behavior is due to the ability of the material to undergo molecular rearrangements and deformations in response to the applied electric field. This performance is usually observed in viscoelastic materials, polymers, and ionic liquids [40]. Figure 13b shows the frequency dependence of the imaginary part of the electric modulus M″ of $Na_{1.5}Mn^{II}{}_3Fe^{III}{}_{0.5}(AsO_4)_3$. The M″ curve shows a broad peak that rises as the temperature increases until reaching a maximum at

296 K, for a frequency of $f_{max} \approx 0.5 \times 10^6$ Hz, approximately. For higher temperatures, this maximum shifts to higher frequencies. When the frequency is between 10^2 and 10^4 Hz, Na^+ ions can move across large distances. However, when the frequency is higher than f_{max}, Na^+ ions are limited to their potential well. As temperature rises, the mobility of the charge carriers increases, causing a decrease in the relaxation time and a shift of the relaxation peak, toward higher frequencies. This phenomenon indicates a dielectric relaxation process, predominantly governed by a hopping mechanism of the charge carriers, which is thermally activated [41].

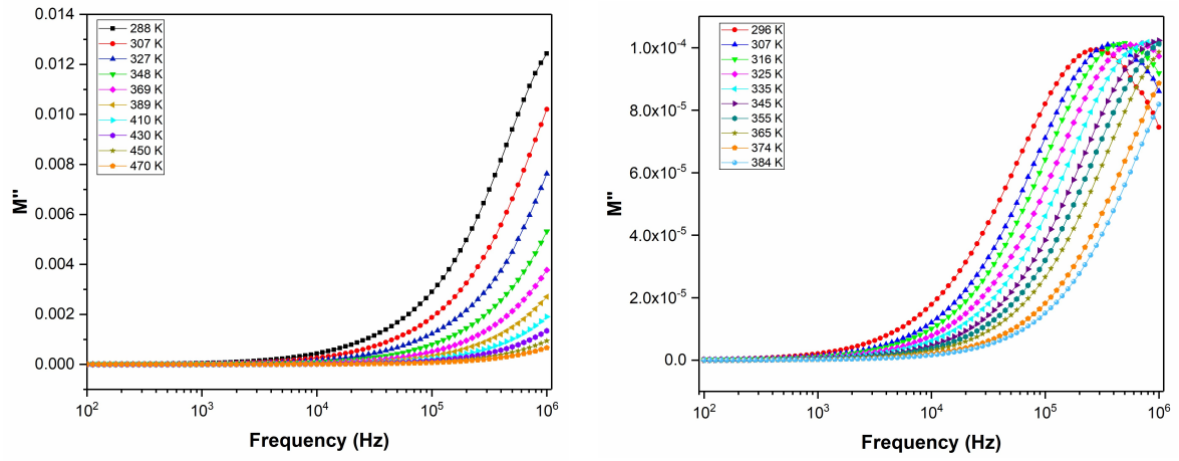


Figure 13. Frequency dependence of the imaginary part of electric modulus for (**a**) $Na_{1.5}Mn^{II}{}_3Mn^{III}{}_{0.5}(AsO_4)_3$ and (**b**) $Na_{1.5}Mn^{II}{}_3Fe^{III}{}_{0.5}(AsO_4)_3$ at different temperatures.

3.9.3. AC Conductivity Study

To analyze the conductivity of both samples, Equation (1) was used to calculate the ac conductivity for each temperature:

$$\sigma_{ac} = \varepsilon_0 \omega \varepsilon'' = \varepsilon_0 \omega \frac{Z'}{C_0 \omega \left(Z'^2 + Z''^2 \right)} = \left(\frac{L}{S} \right) \left(\frac{Z'}{Z'^2 + Z''^2} \right) \quad (1)$$

The real and imaginary parts of the impedance, Z' and Z'', were used along with the thickness, L, and cross-section, S, of the sample to derive the conductivity [42,43]. Figure 13 shows the plots of the ac conductivity of $Na_{1.5}Mn^{II}{}_3Mn^{III}{}_{0.5}(AsO_4)_3$ and $Na_{1.5}Mn^{II}{}_3Fe^{III}{}_{0.5}(AsO_4)_3$ as a function of frequency. An almost frequency-independent behavior is observed for the sample $Na_{1.5}Mn^{II}{}_3Mn^{III}{}_{0.5}(AsO_4)_3$. There is a slight dispersion in the higher frequency region, but the most characteristic feature is the increase in the conductivity with the temperature, revealing a thermal activation phenomenon. Figure 14b shows a relaxation phenomenon, which maximally shifts to higher frequencies with the rise of the temperature.

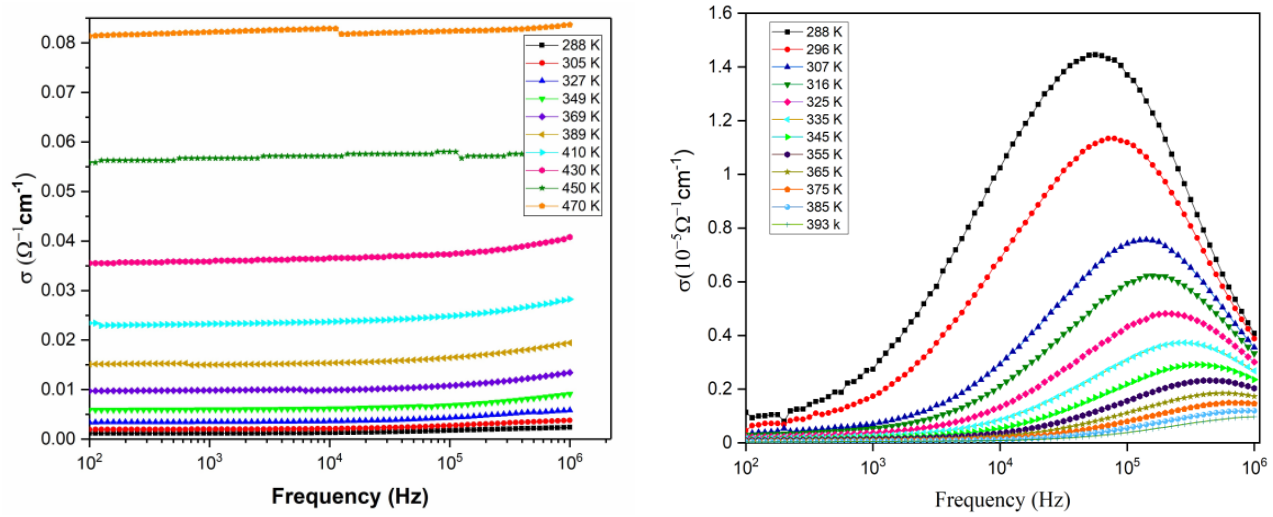


Figure 14. Frequency dependence of the AC conductivity for (**a**) $Na_{1.5}Mn^{II}{}_3Mn^{III}{}_{0.5}(AsO_4)_3$ and (**b**) $Na_{1.5}Mn^{II}{}_3Fe^{III}{}_{0.5}(AsO_4)_3$ at different temperatures.

4. Conclusions

The crystal structures of $Na_{1.5}Mn^{II}{}_3Mn^{III}{}_{0.5}(AsO_4)_3$ and $Na_{1.5}Mn^{II}{}_3Fe^{III}{}_{0.5}(AsO_4)_3$ have been successfully determined and refined. Both compounds crystallize in the monoclinic system with the space group $P2_1/c$. The structural models were validated using bond valence calculations and charge distribution analysis, confirming their accuracy. The analysis revealed that the Mn^{II} and Mn^{III} ions exhibit deviations in their charges, indicating a mixed valence and electron delocalization within the three-dimensional network. The obtained structures consist of interconnected chains of Mn^{II} and Mn^{III} or Fe^{III} octahedra, with AsO_4 tetrahedra connecting them, forming a three-dimensional anionic framework. The presence of tunnels and cavities within the structure allows for the localization of Na^+ cations. The electrical properties were investigated using impedance spectroscopy measurements. The impedance study showed a relaxation phenomenon and a decrease in resistance with increasing temperature. The dielectric modulus (M*) and the AC conductivity were also analyzed, providing insights into the conduction and energy storage properties of the materials.

Author Contributions: Conceptualization, E.R., N.O. and M.P.F.G.; methodology, E.R., S.R.G., J.P.F.C. and S.S.T.; software, E.R. and J.P.F.C.; validation, N.O., M.P.F.G. and S.S.T.; formal analysis, M.P.F.G. and S.S.T.; investigation, E.R., N.O. and M.P.F.G.; resources, M.P.F.G.; data curation, S.R.G. and S.S.T.; writing—original draft preparation, E.R.; writing—review and editing, S.R.G., M.P.F.G. and S.S.T.; visualization, E.R.; supervision, M.P.F.G.; project administration, M.P.F.G.; funding acquisition, N.O. and M.P.F.G. All authors have read and agreed to the published version of the manuscript.

Funding: The authors extend their appreciation to the FEDER funds through the COMPETE 2020 Program and National Funds through FCT—Portuguese Foundation for Science and Technology under the project LISBOA-01-0247-FEDER-039985/POCI-01-0247-FEDER-039985, LA/P/0037/2020, UIDP/50025/2020, and UIDB/50025/2020 of the Associate Laboratory Institute of Nanostructures, Nanomodelling, and Nanofabrication—i3N., UCIBIO (UIDP/04378/2020 and UIDB/04378/2020) and Associate Laboratory i4HB (LA/P/0140/2020). S.R. Gavinho acknowledge FCT—Portuguese Foundation for Science and Technology for the PhD grant (SFRH/BD/148233/2019).

Institutional Review Board Statement: Not applicable.

Informed Consent Statement: Not applicable.

Data Availability Statement: Not applicable.

Acknowledgments: The authors extend their appreciation to the FEDER funds through the COMPETE 2020 Program and National Funds through FCT—Portuguese Foundation for Science and Technology under the projects LISBOA-01-0247-FEDER-039985/POCI-01-0247-FEDER-039985, LA/P/0037/2020, UIDP/50025/2020, and UIDB/50025/2020 of the Associate Laboratory Institute of Nanostructures, Nanomodelling, and Nanofabrication—i3N. S.R. Gavinho acknowledges FCT—Portuguese Foundation for Science and Technology for the PhD grant (SFRH/BD/148233/2019).

Conflicts of Interest: The authors declare no conflict of interest.

References

1. Imai, H.; Kamiya, Y.; Okuhara, T. Selective Oxidation of N-Butane over Nanosized Crystallites of $(VO)_2P_2O_7$ Synthesized by an Exfoliation-Reduction Process of $VOPO_4{\cdot}2H_2O$ in a Mixture of 2-Butanol and Ethanol. *J. Catal.* **2007**, *251*, 195–203. [CrossRef]
2. Jouini, A.; Gâcon, J.C.; Ferid, M.; Trabelsi-Ayadi, M. Luminescence and Scintillation Properties of Praseodymium Poly and Diphosphates. *Opt. Mater.* **2003**, *24*, 175–180. [CrossRef]
3. Herle, P.S.; Ellis, B.; Coombs, N.; Nazar, L.F. Nano-Network Electronic Conduction in Iron and Nickel Olivine Phosphates. *Nat. Mater.* **2004**, *3*, 147–152. [CrossRef] [PubMed]
4. Daidouh, A.; Durio, C.; Pico, C.; Veiga, M.L.; Chouaibi, N.; Ouassini, A. Structural and Electrical Study of the Alluaudites $(Ag_1 - xNax)_2FeMn_2(PO_4)_3$ (x = 0, 0.5 and 1). *Solid State Sci.* **2002**, *4*, 541–548. [CrossRef]
5. Bdey, S.; Savvin, S.N.; Bourguiba, N.F.; Núñez, P. Synthesis, Crystal Structure and Na+ Transport in $Na_3La(AsO_4)_2$. *J. Solid State Chem.* **2022**, *305*, 122644. [CrossRef]
6. Masquelier, C.; Patoux, S.; Wurm, C.; Morcrette, M. Polyanion-Based Positive Electrode Materials. In *Lithium Batteries*; Springer: Boston, MA, USA, 2009; ISBN 978-0-387-92675-9_15.
7. Moore, P.B.; Ito, J. Wyllieite, Na_2Fe^{2+} $2Al[PO_4]_3$, a New Species. *Mineral. Rec.* **1973**, *4*, 131–136.
8. Moore, P.B.; Ito, J. Alluaudites, Wyllieites, Arrojadites: Crystal Chemistry and Nomenclature. *Miner. Mag.* **1979**, *43*, 227–235. [CrossRef]
9. Yang, H.; Downs, R.T.; Gu, X.; Xie, X.; Kobsch, A. Fupingqiuite, IMA 2016-087. CNMNC Newsletter No. 35. *Miner. Mag.* **2017**, *81*, 209–213.
10. Frigui, W.; Zid, M.F.; Driss, A. Wyllieite-Type $Ag_{1.09}Mn_{3.46}(AsO_4)_3$. *Acta Crystallogr. Sect. E Struct. Rep. Online* **2012**, *68*, i40–i41. [CrossRef]
11. Frigui, W.; Zid, M.F.; Driss, A. Synthesis and Physico-Chemical Study of $Na_{0.5}K_{0.65}Mn_{3.43}(AsO_4)_3$ Compound. *Jordan J. Chem.* **2011**, *6*, 295–305.
12. Marzouki, R.; Ben Smida, Y.; Avdeev, M.; Alghamdi, M.M.; Zid, M.F. Synthesis, Structure and Na+ Migration Pathways of New Wylleite-Type $Na_{1.25}Co_{2.187}Al_{1.125}(AsO_4)_3$. *Mater. Res. Express* **2019**, *6*, 126313. [CrossRef]
13. Bdey, S.; Bourguiba, N.F.; Savvin, S.N.; Núñez, P. $Na_3Bi(AsO_4)_2$: Synthesis, Crystal Structure and Ionic Conductivity. *J. Solid State Chem.* **2019**, *272*, 189–197. [CrossRef]
14. Degen, T.; Sadki, M.; Bron, E.; König, U.; Nénert, G. The High Score Suite. *Powder Diffr.* **2014**, *29*, S13–S18. [CrossRef]
15. Chen, H.; Wong, L.L.; Adams, S. SoftBV—A Software Tool for Screening the Materials Genome of Inorganic Fast Ion Conductors. *Acta Crystallogr. Sect. B Struct. Sci.* **2019**, *75*, 18–33. [CrossRef]
16. Momma, K.; Izumi, F. VESTA 3 for Three-Dimensional Visualization of Crystal, Volumetric and Morphology Data. *J. Appl. Crystallogr.* **2011**, *44*, 1272–1276. [CrossRef]
17. Teixeira, S.S.; Graça, M.P.F.; Lucas, J.; Valente, M.A.; Soares, P.I.P.; Lança, M.C.; Vieira, T.; Silva, J.C.; Borges, J.P.; Jinga, L.I.; et al. Nanostructured $LiFe_5O_8$ by a Biogenic Method for Applications from Electronics to Medicine. *Nanomaterials* **2021**, *11*, 193. [CrossRef]
18. Graça, M.P.F.; Ferreira da Silva, M.G.; Sombra, A.S.B.; Valente, M.A. Electric and Dielectric Properties of a SiO_2-Na_2O-Nb_2O_5 Glass Subject to a Controlled Heat-Treatment Process. *Phys. B Condens. Matter* **2007**, *396*, 62–69. [CrossRef]
19. Graça, M.P.F.; Prezas, P.R.; Costa, M.M.; Valente, M.A. Structural and Dielectric Characterization of $LiNbO_3$ Nano-Size Powders Obtained by Pechini Method. *J. Solgel. Sci. Technol.* **2012**, *64*, 78–85. [CrossRef]
20. Graça, M.P.F.; Ferreira da Silva, M.G.; Valente, M.A. $NaNbO_3$ Crystals Dispersed in a B_2O_3 Glass Matrix—Structural Characteristics versus Electrical and Dielectrical Properties. *Solid State Sci.* **2009**, *11*, 570–577. [CrossRef]
21. Toby, B.H. EXPGUI, a Graphical User Interface for GSAS. *J. Appl. Crystallogr.* **2001**, *34*, 210–213. [CrossRef]
22. Toby, B.H. R Factors in Rietveld Analysis: How Good Is Good Enough? *Powder Diffr.* **2006**, *21*, 67–70. [CrossRef]
23. Adams, S. Structural Science Relationship between Bond Valence and Bond Softness of Alkali Halides and Chalcogenides. *Acta Crystallogr. Sect. B Struct. Sci.* **2001**, *B57*, 278–287. [CrossRef]
24. Brown, I.D.; Shannon, R.D. Empirical Bond-strength–Bond-length Curves for Oxides. *Acta Crystallogr. Sect. A* **1973**, *29*, 266–282. [CrossRef]
25. Yakubovich, O.V.; Massa, W.; Gavrilenko, P.G.; Dimitrova, O.V. The Crystal Structure of a New Synthetic Member in the Wyllieite Group: $Na_{1.265}Mn^{2+}{}_{2.690}Mn^{3+}{}_{0.785}(PO_4)_3$. *Eur. J. Mineral.* **2005**, *17*, 741–748. [CrossRef]
26. Ayed, B.; Krifa, M.; Haddad, A. $Na_{1.72}Mn_{3.28}(AsO_4)_3$. *Acta Crystallogra. Sect C Cryst. Struct. Commun.* **2002**, *58*, i98–i100. [CrossRef]

27. Shannon, R.D.; Prewitt, C.T. Effective Ionic Radii in Oxides and Fluorides. *Acta Crystallogr. Sect. B Struct. Sci.* **1969**, *25*, 925–946. [CrossRef]
28. Ouaatta, S.; Assani, A.; Saadi, M.; El Ammari, L. Crystal Structure of a New Tripotassium Hexanickel Iron Hexaphosphate. *Acta Crystallogr. Sect. E Struct. Rep. Online* **2019**, *75*, 402–404. [CrossRef]
29. Nakamoto, K. *Infrared and Raman Spectra of Inorganic and Coordination Compounds Part B: Applications in Coordination, Organometallic, and Bioinorganic Chemistry*, 6th ed.; Wiley: Hoboken, NJ, USA, 2009; ISBN 978-0-471-74493-1.
30. Augsburger, M.S.; Juri, M.A.; Pedregosa, J.C.; Mercader, R.C. Crystal Data and Spectroscopic Studies of $NaNiFe_2(AsO_4)_3$. *J. Solid State Chem.* **1992**, *101*, 66–70. [CrossRef]
31. Frost, R.L.; Čejka, J.; Sejkora, J.; Plášil, J.; Bahfenne, S.; Palmer, S.J. Raman Microscopy of the Mixite Mineral $BiCu_6(AsO_4)_3(OH)_6{\cdot}3H_2O$ from the Czech Republic. *J. Raman Spectrosc.* **2009**, *41*, 566–570. [CrossRef]
32. Khorari, S.; Rulmont, A.; Cahay, R.; Tarte, P. Structure of the Complex Arsenates $NaCa_2M_{2+2}(AsO_4)3$ (M_{2+} = Mg, Ni, Co): First Experimental Evidence of a Garnet-Alluaudite Reversible Polymorphism. *J. Solid State Chem.* **1995**, *118*, 267–273. [CrossRef]
33. Khorari, S.; Rulmont, A.; Tarte, P. Alluaudite-Like Structure of the Arsenate $Na_3In_2(AsO_4)_3$. *J. Solid State Chem.* **1997**, *134*, 31–37. [CrossRef]
34. Kawabe, Y.; Yabuuchi, N.; Kajiyama, M.; Fukuhara, N.; Inamasu, T.; Okuyama, R.; Nakai, I.; Komaba, S. Synthesis and Electrode Performance of Carbon Coated Na_2FePO_4F for Rechargeable Na Batteries. *Electrochem. Commun.* **2011**, *13*, 1225–1228. [CrossRef]
35. Rajah, F.; Graia, M.; Mhiri, T. Synthesis, Crystal Structure, and Characterization of $Na_7Cu_4(AsO_4)_5$. *Phosphorus Sulfur Silicon Relat. Elem.* **2013**, *188*, 1244–1253. [CrossRef]
36. Priestner, M.; Singer, G.; Weil, M.; Kremer, R.K.; Libowitzky, E. Synthesis, Structural, Magnetic and Thermal Properties of $Mn_2As_2O_5$, the First Pyro-Arsenite of a First-Row Transition Metal. *J. Solid State Chem.* **2019**, *277*, 209–215. [CrossRef]
37. Behera, B.; Nayak, P.; Choudhary, R.N.P. Impedance Spectroscopy Study of $NaBa_2V_5O_{15}$ Ceramic. *J. Alloys Compd.* **2007**, *436*, 226–232. [CrossRef]
38. Costa, M.M.; Pires, G.F.M.; Terezo, A.J.; Graa, M.P.F.; Sombra, A.S.B. Impedance and Modulus Studies of Magnetic Ceramic Oxide $Ba_2Co_2Fe_{12}O_{22}(Co_2Y)$ Doped with Bi_2O_3. *J. Appl. Phys.* **2011**, *110*, 034107. [CrossRef]
39. Sohn, R.S.T.M.; Macêdo, A.A.M.; Costa, M.M.; Mazzetto, S.E.; Sombra, A.S.B. Studies of the Structural and Electrical Properties of Lithium Ferrite ($LiFe_5O_8$). *Phys. Scr.* **2010**, *82*, 055702. [CrossRef]
40. Kumar, A.; Singh, B.P.; Choudhary, R.N.P.; Thakur, A.K. Characterization of Electrical Properties of Pb-Modified $BaSnO_3$ Using Impedance Spectroscopy. *Mater. Chem. Phys.* **2006**, *99*, 150–159. [CrossRef]
41. Lily; Kumari, K.; Prasad, K.; Choudhary, R.N.P. Impedance Spectroscopy of $(Na_{0.5}Bi_{0.5})(Zr_{0.25}Ti_{0.75})O_3$ Lead-Free Ceramic. *J. Alloys Compd.* **2008**, *453*, 325–331. [CrossRef]
42. Lu, W.; Jiang, S.; Zhou, D.; Gong, S. Structural and Electrical Properties of $Ba(Sn,Sb)O_3$ Electroceramics Materials. *Sens. Actuators A* **2000**, *80*, 35–37. [CrossRef]
43. Iben Nassar, K.; Rammeh, N.; Teixeira, S.S.; Graça, M.P.F. Physical Properties, Complex Impedance, and Electrical Conductivity of Double Perovskite $LaBa_{0.5}Ag_{0.5}FeMnO_6$. *J. Electron. Mater.* **2022**, *51*, 370–377. [CrossRef]

Disclaimer/Publisher's Note: The statements, opinions and data contained in all publications are solely those of the individual author(s) and contributor(s) and not of MDPI and/or the editor(s). MDPI and/or the editor(s) disclaim responsibility for any injury to people or property resulting from any ideas, methods, instructions or products referred to in the content.